International Journal of Applied Earth Observation and Geoinformation 123 (2023) 103445

Contents lists available at ScienceDirect

International Journal of Applied Earth Observation and Geoinformation

journal homepage: www.elsevier.com/locate/jag

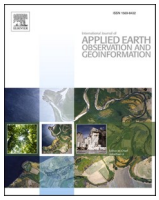

Automatic seismic source modeling of InSAR displacements

Simone Atzori [a,*], Fernando Monterroso [b], Andrea Antonioli [a], Claudio De Luca [b], Nikos Svigkas [a], Francesco Casu [b], Michele Manunta [b], Matteo Quintiliani [a], Riccardo Lanari [b]

[a] Istituto Nazionale di Geofisica e Vulcanologia, Rome, Italy
[b] Istituto per il Rilevamento Elettromagnetico dell'Ambiente, Naples, Italy

ARTICLE INFO

Keywords:
InSAR
Earthquake modeling
Real-time analysis
Automatic processing
Fault scaling factors
Data analysis
Algorithms and implementation
Satellite geodesy: results
Tectonic deformation
Earthquake source observations

ABSTRACT

In this work we describe the implementation of a processing chain for a fully automatic modeling of the seismic source parameters and its slip distribution through the inversion of the InSAR displacements generated from the EPOSAR service. This processing chain consists of a suite of procedures and algorithms handling a sequence of steps: selection of the highest quality InSAR datasets, definition of the area of interest, image sampling, non-linear and linear inversions to get, respectively, the source geometry and its slip distribution. A set of side procedures and interfaces also allows an interactive refinement and the publication of results, consisting of scientific data and graphical outputs. The whole procedure has been developed, tested and validated by considering 100 events with magnitudes between 5.5 and 8.2, worldwide distributed and covering an exhaustive range of mechanisms and tectonic contexts.

Main aim of this work is describing the implementation of the automatic modeling procedures, used to produce solutions in real time, already during the emergency phase. These sources, validated by experts before their publication, can be a reference for operational purposes and initial scientific analyses. The creation of this repository sets also the framework to store, out of the emergency time, more sophisticated solutions, manually revised and/or with peer-review quality.

1. Introduction

Automatic procedures are created to provide unsupervised results based on consolidated and robust algorithms, minimizing the processing time and the need of an interaction with an expert operator. In real-time monitoring of earthquakes, for instance, the analysis of P-S arrival times and of seismic waves allows to quickly derive the event location, its magnitude and the rupture mechanism, through the calculation of the full moment tensor.

At the same time, thanks to decades of algorithm improvements and to the availability of an unprecedented treasure trove of free Synthetic Aperture Radar (SAR) satellite data acquired by the Sentinel-1 constellation of the Copernicus Program (Torres et al, 2012), the ability of measuring the permanent deformations induced by an earthquake allowed the growth of services that automatically provide displacement maps generated through the Differential SAR Interferometry (InSAR, hereinafter) technique (Gabriel et al., 1989). Examples of available services delivering automatic InSAR maps after an event, at global scale, are: LiCS (Looking inside the Continents from Space) implemented at the Centre for Observation and Modelling of Earthquakes, Volcanoes and Tectonics (COMET, UK, https://comet.nerc.ac.uk/comet-lics-portal/); ARIA, the Advanced Rapid Imaging and Analysis project from a collaboration between Jet Propulsion Laboratory (JPL, California) and Caltech, the California Institute of Technology (web portal: https://aria.jpl.nasa.gov/index.html); the GeObservatory service from BEYOND, Center for Earth Observation Research and Satellite Remote Sensing of the National Observatory of Athens (http://geobservatory.beyond-eocenter.eu/) and the EPOSAR service from IREA-CNR (https://geohazards-tep.eu/geobrowser/?id=epos), acting within the umbrella of the EPOS (European Plate Observing System) platform (web portal: https://www.ics-c.epos-eu.org/).

InSAR displacements have been widely used, since the first astonishing results for the 1992 Landers earthquake (Massonnet et al, 1993), to investigate the characteristics of a seismic source; among various approaches, modeling the observed deformations exploiting analytical equations and optimisation algorithms is the most diffused, since it provides most of the fault information in the shortest possible time, with results that can be exploited already during the emergency phase (Atzori

* Corresponding author at: Via di Vigna Murata, 605, 00143 Rome, Italy.
E-mail address: simone.atzori@ingv.it (S. Atzori).

https://doi.org/10.1016/j.jag.2023.103445
Received 14 April 2023; Received in revised form 28 July 2023; Accepted 1 August 2023
Available online 18 August 2023

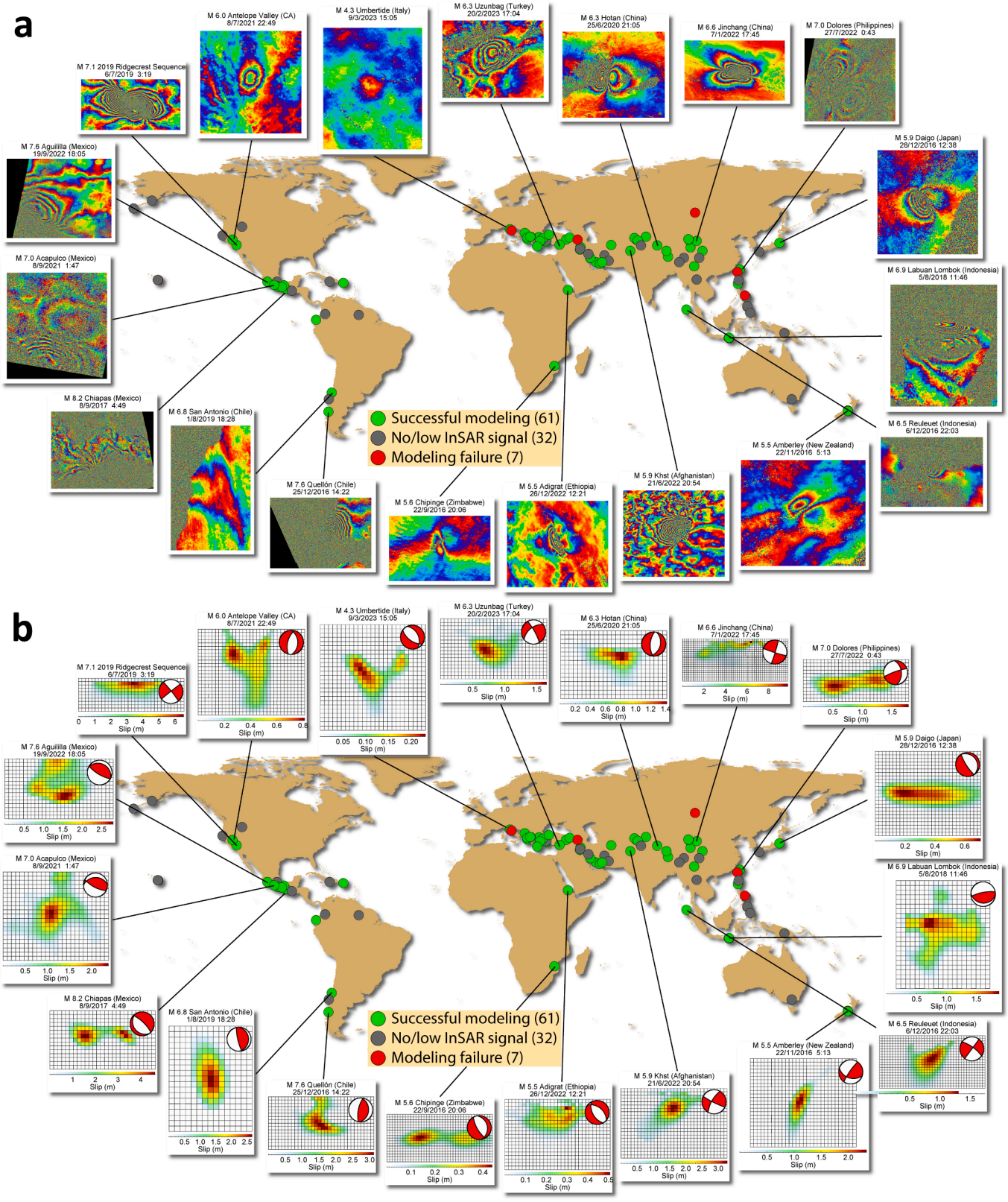

Fig. 1. Map of the 100 events processed in this work, with some examples of interferograms (**a**) and slip distributions (**b**) obtained through automatic modeling. In Table 1, Supplementary Fig. S1 and the page http://terremoti.ingv.it/finitesource the complete database of finite sources derived from InSAR-EPOSAR displacements. Details about positive and negative outcomes will be presented in the discussion section with the algorithm performance.

and Salvi, 2014).

In this work we capitalize twenty years of algorithm implementation in source modeling and the collaboration between two Italian public research institutions, INGV (Istituto Nazionale di Geofisica e Vulcanologia) and CNR-IREA (Consiglio Nazionale delle Ricerche - Istituto per il Rilevamento Elettromagnetico dell'Ambiente), to set up a processing chain that automatically performs the source modeling after the availability of every new EPOSAR product, generated for a specific earthquake.

Modeling is therefore triggered from the EPOSAR service, which is, in turn, triggered by the occurrence of an earthquake above M 5.5 worldwide, as described in the next section. The whole chain is intended to generate real-time products that are made available to Civil Protection authorities and to the scientific community. Solutions, made available in a public repository, are marked as "automatic" or "revised", if validated and refined by a scientist.

Hundred events are used to develop and test this processing chain, where consolidated models and algorithms are wrapped with new ones that automatically handle the whole process, from the image selection and sampling to the data inversion and distributed slip calculation (Fig. 1).

The processing and archiving of this initial dataset also opens the way to the construction of a complete database of seismic sources for the events that occurred during the operational time of the Sentinel-1 constellation, i.e. from 2014. Though the 100 events have been handled as they were produced in real time, when other source models from geodetic data are not available, the repository will be possibly exploited to share high-quality, peer-reviewed sources, that will be opportunely marked and will replace real-time data. At the writing time, the database completion and the web service implementation are under development, but a web page to access the sources from the 100 event dataset is already available at http://terremoti.ingv.it/finitesource.

We further remark that several repositories already exist that freely offer to the community earthquake source models. We mention here, as examples, the models of some major earthquakes provided from Caltech (http://www.tectonics.caltech.edu/slip_history/index.html), from the University of California–Santa Barbara (http://www.geol.ucsb.edu/faculty/ji/big_earthquakes/home.html) and earthquake models of some earthquakes from the University of Tsukuba (http://www.geol.tsukuba.ac.jp/~yagi-y/eng/earthquakes.html). A rich database of finite-fault rupture models of past earthquakes models is maintained in SRCMOD (http://equake-rc.info/srcmod; Mai and Thingbaijam, 2014). Slip distributions for important events, based on seismological and, more recently, also on geodetic data, can be found also in the United States Geological Survey (USGS) seismic catalog (https://www.usgs.gov/programs/earthquake-hazards/earthquakes).

Following the evolution of the EPOSAR service, the catalog of sources will also include solutions derived from future SAR missions with open access policy (e.g. the incoming NASA-ISRO SAR, NISAR, mission). The automatic modeling chain has been implemented with a set of graphical interfaces that allow the elaboration of InSAR data coming from every service or software.

As final comment, open issues still remain to solve, as the difficulty of generating automatic solutions for particularly complex sources, when more segments are activated or when more events occur, close in space and time. We address all these aspects later in this work.

2. InSAR data automatic processing: The EPOSAR service

The European Plate Observing System is a pan-European research infrastructure that provides and facilitates access to data collections from the solid Earth scientific community (EPOS, 2022). EPOS is organized in communities represented within the Thematic Core Services (TCS), such as Seismology, Near-Fault Observatories, GNSS data, Volcano Observations, Satellite Data, Geomagnetic Observations, Anthropogenic Hazards, Geological Information and Modelling. Among all, the TCS Satellite Data (SATD) allows the scientific community to access and download advanced satellite products generated over selected areas as well as to remotely process satellite datasets.

In particular, the TCS SATD deploys a service, referred to as EPOSAR, implemented by the Institute for Electromagnetic Sensing of Environment (IREA) of National Research Council (CNR) (Italy), that generates real-time InSAR co-seismic interferograms and Line-of-Sight (LoS) displacement maps every time a significant earthquake occurs, in a completely automated way (Monterroso et al, 2019; Monterroso et al., 2020). These products are nowadays generated by exploiting the rich spaceborne SAR data archives acquired by the Sentinel-1 constellation (Torres et al 2012).

In particular, to generate InSAR co-seismic products, the implemented EPOSAR service queries two different earthquake catalogs (USGS and INGV) that trigger the InSAR processing; after the occurrence of an event, the processing is performed every time a new S1 image for the interested area gets available. InSAR processing is carried out through the Parallel Small BAseline Subsets (P-SBAS) algorithm (Casu et al 2014; Manunta et al 2019), which has been adapted to optimize the unwrapping step (Fornaro et al 1997; Costantini and Rosen 1999) that is now only applied to the part of the InSAR interferograms delimited by the area identified through a predicted deformation scenario and not to the whole S1 scene. This task is achieved by using the retrieved focal mechanism as provided by the USGS or INGV earthquake catalogs. Moreover, the EPOSAR service may also benefit from the computing resources available through Cloud Computing environments (Monterroso et al., 2022). Taking advantage of these computing resources, the developed tool has been used not only to operationally investigate every new earthquake, but also to process all the InSAR data dating back to the first available S1 acquisition. Accordingly, a complete archive of the co-seismic products related to all the significant earthquakes that occurred since 2015 has been generated (Monterroso et al 2020; Monterroso et al., 2022) and is available at https://store.terradue.com/gep-epos-datarepo/EPOSAR/S1/. The global scale availability of SAR data has allowed us a massive production of co-seismic interferograms (about 9600) investigating 561 earthquakes, at the writing time.

3. Overview of the source modeling algorithm implementation

In our implementation, data modeling is carried out with a consolidated two-step approach: a first non-linear optimization to define the fault location, geometry and rupture mechanism with uniform slip, followed by a linear inversion to determine the dislocation distribution on the fault plane (Wright et al, 2003; Atzori et al, 2009); in both cases, the underlying model is the rectangular shear dislocation in an homogeneous half-space (Okada, 1985), used as uniform-slip source for the non-linear inversion, and as two-dimensional array of sources to simulate the slip distribution. In addition to the automatization of inversion procedures, we also implemented several algorithms to fully cover every step of the modeling process, including for instance the selection of the best InSAR datasets to ingest and their sampling.

To focus on the area to investigate, the process starts with the exploitation of a focal mechanism, as explained later in detail. It is known that hypocenters and moment tensors, however, could be affected by horizontal and/or vertical shifts (Weston et al., 2012); we therefore implemented the non-linear inversion with a two-level accuracy:

- *coarse inversion*: it is the first non-linear inversion, based on any available focal mechanism that can be accessed through web services (from USGS, for most of the cases, but also from INGV);
- *refined inversion*: it is based on the source model obtained with the coarse inversion; this guarantees that this second non-linear inversion step is perfectly centered on the area affected by the coseismic displacement. The refined inversion is executed only if the coarse inversion successfully ended.

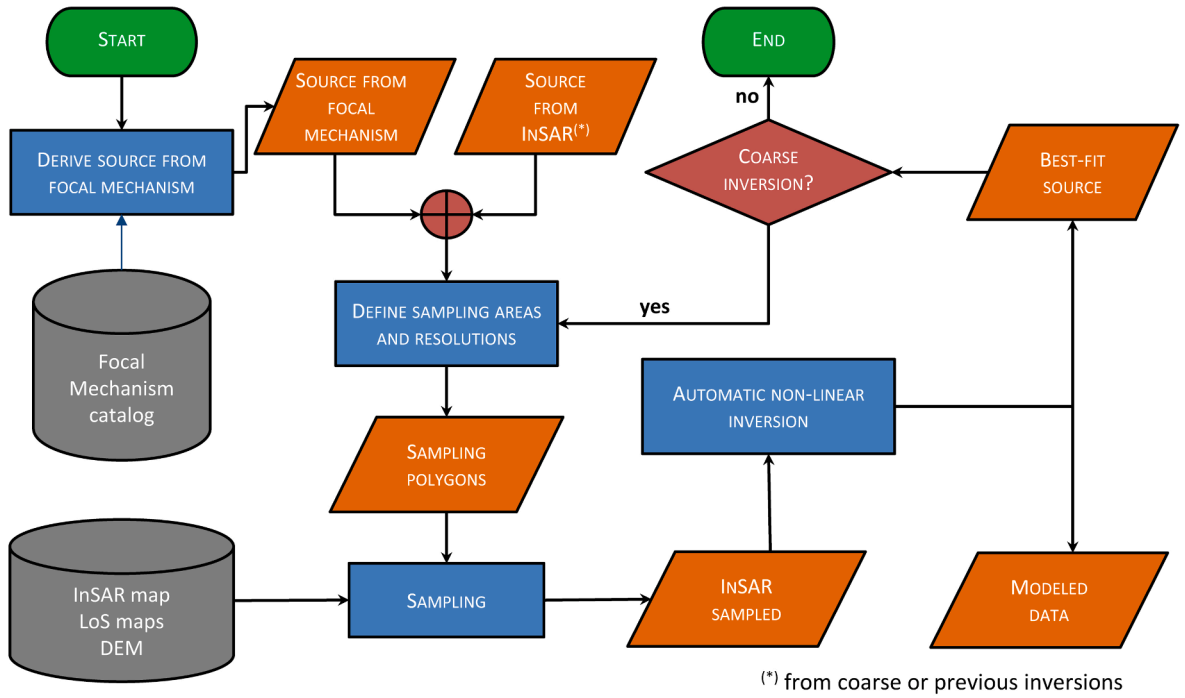

Fig. 2. Flow-chart of the non-linear automatic inversion, summarizing the two-level approach: a first coarse inversion based on the focal mechanism and a second refined inversion, based on the results of the coarse one. The "Automatic non-linear inversion" element is described in detail in Fig. 4.

In Fig. 2 a flow chart of the non-linear inversion scheme, preceded by pair selection and image sampling, is shown. Since the whole procedure automatically starts from a focal mechanism, and it is not possible to *a priori* discriminate the real from the auxiliary plane, the complete processing chain described in the following sections are entirely repeated for both planes. In the analysis of the algorithm performance, we discuss how the ambiguity between the real and the auxiliary planes is managed.

After a successful end of the non-linear inversion, a linear inversion is carried out to retrieve the slip distribution, as also explained later in a specific section.

We remark that the whole system is explicitly implemented to update the model in accordance to the availability of InSAR displacements, i.e. when new satellite acquisitions get available; the whole process is repeated when new displacement maps are provided from the EPOSAR service, but previous results are exploited to refine the solution instead of starting the modeling from scratch.

4. InSAR displacements setup

4.1. Sampling areas and resolutions

As introduced in the previous section, raster displacement maps need to be sampled to reduce the number of points handled by the inversion. This task also requires an automatic way to define the area of interest, since the displacement field is generally smaller than a whole InSAR frame.

The first attempt to define the area to investigate is based on a focal mechanism, automatically retrieved from the USGS Earthquake Hazards Program or the INGV web services. By applying the scaling factor of Leonard et al., (2010), we derive the finite source and, after forward modeling, a displacement scenario; this scenario allows the definition of a bounding box, that is initially sampled with a uniform mesh to generate the input datasets for the first coarse inversion.

For the refined inversion, the area of interest is still based on a

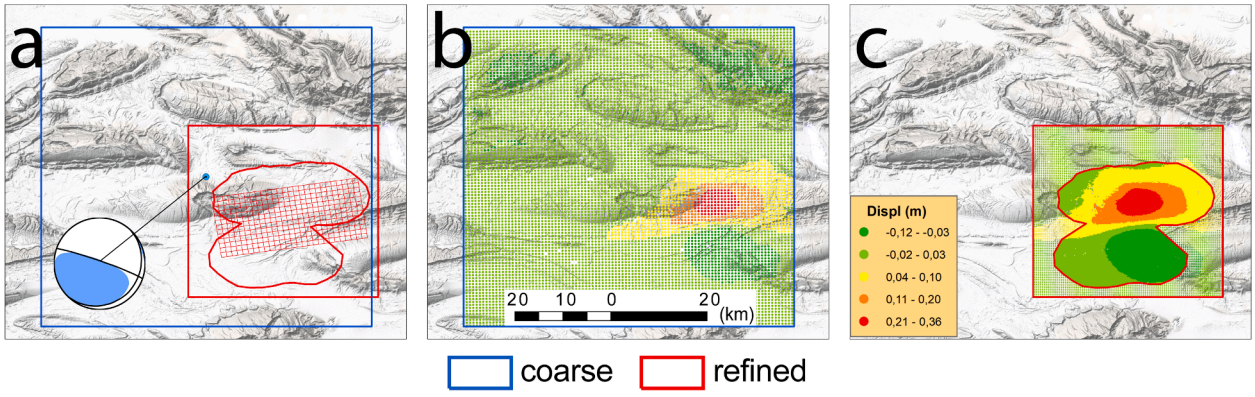

Fig. 3. Polygons used to sample InSAR maps, based on a scenario derived from the USGS focal mechanism and scaling factors (blue polygon in **a** and points, sampled every 608 m, in **b**) and the scenario built after the coarse inversion (red polygons in **a**, with points in c, sampled every 349 and 174 m, in the far and near field, respectively). The red mesh in **a** describes the final fault location after automatic modeling. Data refer to the November 14, 2021, Bandar Abbas (Iran), M 6.4 event. Datasets sampled before the coarse and refined inversions are stored in an ESRI point-shapefile.

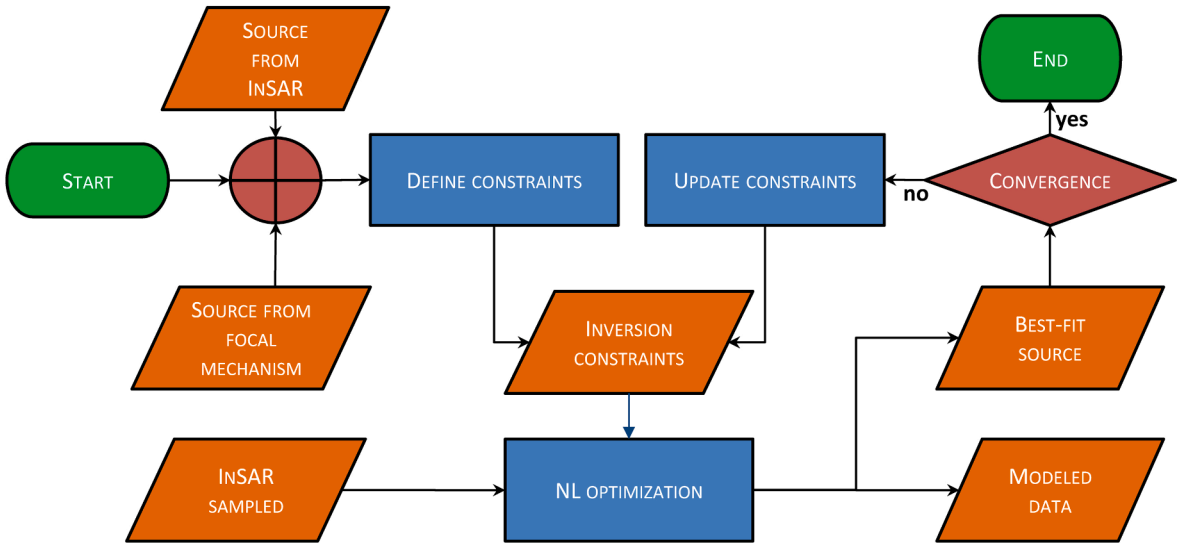

Fig. 4. Detailed flowchart of the *Automatic non-linear inversion* element in Fig. 2. This flowchart describes in detail the sequence of procedures implemented to get the best-fit source. The *Update constraints* procedure decides if and how input parameters must be updated.

predicted scenario, but built upon the source obtained from the coarse inversion and, therefore, already matching the observed displacement. In this case, a two-level sampling is adopted: a polygon enclosing the near field, affected by significant displacements, and an outer rectangle enclosing it. Criteria to define the near field are inherently problem-dependent and the sampling resolution in the near field is set double of the outer rectangle. The improvement achieved from the coarse to the refined inversion can be significant, as shown in Fig. 3, and it also addresses the analysis of systematic shifts that could be found between seismological and InSAR-based source parameters, as discussed in the Perspectives and Conclusions section.

After the availability of any new InSAR dataset for the same event, the definition of the sampling area for the coarse inversion is based on the last modeled source, instead of a focal mechanism and scaling factors. As previously highlighted, this makes the whole system capable to update the solution instead of starting from scratch the modeling, when new interferometric maps are generated.

4.2. InSAR displacement selection

Within the EPOSAR service, InSAR maps are automatically produced by including pre-, co– and post-seismic pairs, according to the availability of Sentinel-1 acquisitions (Monterroso et al., 2020). In particular, for a given track, the EPOSAR service generates several pairs that share the same pre- or post-event, with a high data redundancy. The image selection procedure preliminary discards all the pre- and post-coseismic pairs, then selects the coseismic pairs to sample according to these criteria:

- unless a single orbit is available, the number of ascending and descending orbits used in the inversions must be the same;
- if more than one pair is available from the same track, the one with the shortest temporal baseline is considered;
- when the number of available ascending and descending tracks is different and a selection is necessary according to the first rule, priority is given to those better covering the affected area.

The image selection is performed before the coarse and the refined non-linear inversions, since the scenario based on the focal mechanism could be affected by a significant shift, altering the selection of better centered pairs.

Selected InSAR maps are then sampled for the areas and with the resolutions described in the previous section and results are stored as point-vector in ESRI shapefile format; in addition to the displacement values, the LoS (Line-of-Sight) unit vectors and the topographic elevation are also stored as ancillary information to use in the inversion (Fig. 2). Before running the inversion, point datasets are eventually compared with the water body polygons to remove possible spurious offshore values.

5. Automatic non-linear inversion

The non-linear inversion core, either coarse or refined, consists of a first procedure to define the input inversion constraints (*Define constraints* block in Fig. 4), followed by a group of two procedures, iteratively repeated: the non-linear optimization, to find the best-fit solution according to the given input parameters (*NL optimization* block), and the update of the input constraints (*Update constraints* block). The iteration of these two procedures continues until a convergence is reached.

The *Define constraints* procedure starts by setting the range interval for every source parameter: fault dimension, position, depth, orientation, rake and slip; after the availability of the first InSAR map, these intervals are centered around the focal mechanism values and those of the finite fault derived from scaling factors. Whenever a new InSAR dataset gets available, the *Define constraints* procedures exploits the last inverted model, as already described above for the definition of the sampling area. In addition, an offset (when only one dataset is inverted), or the coefficients of a possible ramp affecting the InSAR phase signal (Manunta et al, 2019), are also set as free parameters to invert for every dataset. The *NL optimization* procedure is then run to get the best-fit source, using the Levemberg-Marquardt optimization scheme (Marquardt, 1963), implemented with multiple restarts to avoid a cost-function minimization with a parameter configuration corresponding to a local minimum.

This best-fit source is then analyzed with the *Update constraints* algorithm; within this procedure the following output conditions are handled:

- at least one of the free parameters reaches its minimum or maximum allowed values: its new input range is updated, centered on the best-fit value;
- the top of the fault reaches the minimum depth: the algorithm calculates the topography at the fault trace and the input depth interval is updated allowing negative values, i.e. above the elastic half-space.

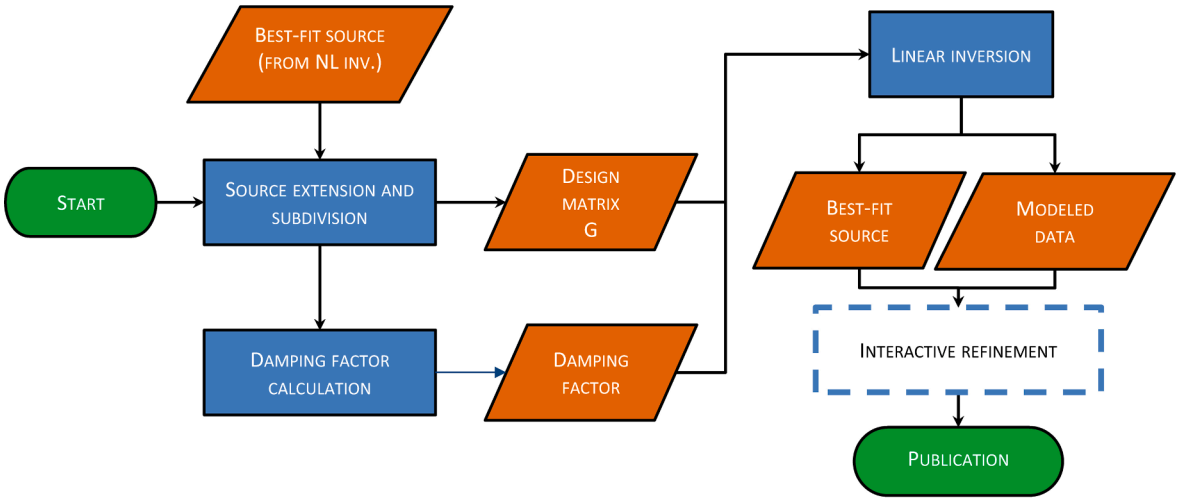

Fig. 5. Linear inversion flow chart. *Ad hoc* algorithms have been implemented for the source extension, its subdivision and for the calculation of the most appropriate damping factor.

The inclusion of topography follows the approach proposed in Williams and Wadge (1998);

- the expected model, according to the focal mechanism, is a low dip source (dip $< 25°$), and the best-fit source differs of more than $10°$: in this case the dip angle is fixed to that of the focal mechanism;
- the best-fit value of the dip is $90°$, suggesting that a better fit could be achieved with a source dipping in the opposite direction; the dip, strike and rake searching intervals are updated, accounting for the switch between footwall and hanging wall;
- a nearly perfect tradeoff between rake and strike is registered, as observed for low-dip sources (Atzori et al. 2019): the rake is constrained to that of the focal mechanism;
- length and/or width assume unreliable small values, showing a nearly perfect tradeoff with the slip: this happens when observations cannot constrain one or both the fault dimensions, in general due to the source depth or the offshore position. When only one dimension is unconstrained (generally, the width) we assume to have a "line-source" condition, becoming "point-source" when both length and width are unconstrained. Under these conditions, the unconstrained parameter is fixed and only the slip is allowed to vary; in this case, abnormal uniform slip values are expected and accepted (this condition will be handled with the linear inversion);
- the source is laterally unconstrained, as in the case of partially or totally offshore locations: length or width are fixed to the value expected from scaling factors.

In order to gradually modify the input update, the three angle (strike, dip and rake) ranges are never modified simultaneously. In addition to the previous rules, and only for the refined inversion, during the iterations the dataset weights are also automatically adjusted, according to the approach described in Atzori et al. (2019).

The *NL optimization* + *Update constraints* sequence is iteratively repeated until one of the following criteria is verified:

1. all the parameters not constrained have best-fit values within their minimum/maximum ranges;
2. the direction of the slip vector, in the 3D space, is too different from that of the focal mechanism (more than $55°$, by default);
3. the maximum number of iterations is reached (30, by default).

Criterion 1 corresponds to a successful non-linear optimization, while criteria 2 and 3 indicate a failure, after which the overall process, for that specific focal plane, is aborted. Possible failure reasons will be discussed later. In the case of convergence to a stable, uniform-slip solution, the process keeps running with the linear inversion to get the slip distribution over the fault plane.

6. Automatic linear inversion

Goal of the linear inversion is to retrieve the distribution of the shear dislocation over the fault plane identified by non-linear inversion. This inversion is preceded by two actions: i) the extension, in length and width, of the non-linear source, to include the whole slip distribution from the peak value to zero, and ii) the fault plane subdivision into a number of patches, each of which will have its own slip value after the linear inversion. The problem is then set up with the usual $\mathbf{d} = \mathbf{Gm}$ linear system, where $\mathbf{m}$ is the vector of slip values, $\mathbf{d}$ is the vector of observations and $\mathbf{G}$ the design matrix based on the same dislocation model in an elastic half-space (Okada, 1985) used in the non-linear optimization. The inversion to find the vector of estimated slip values, $\mathbf{m}^{\mathbf{est}}$, is solved with a damped and constrained least-square approach (Menke, 1989). The overall linear inversion is illustrated in the flow chart of Fig. 5.

6.1. Source extension and subdivision

The extension of the uniform slip source is necessary to define a rectangular plane large enough to accommodate the whole slip distribution. This task must face the large variety of outcomes from the non-linear inversion; as already mentioned, InSAR displacements are not always capable of constraining both fault dimensions: offshore locations, source depth or lack of coverage lead to line- or point-source solutions. Another possible condition to handle is a uniform slip fault reaching the surface, that can be only extended downdip. After a large number of attempts, the best performing algorithm we found is:

1. length and width, regardless of the non-linear outcome, are set as 1.5 times their values from scaling factors; only for subduction zones (dip $< 25°$) and only if the best-fit width is greater than that from scaling factors, we extend 1.5 times the width from non-linear inversion;
2. the fault is symmetrically extended upward, downward and laterally, except when the non-linear source already reaches the topographic surface.

Following the fault extension, the subdivision into equal sub-elements is conducted as follows:

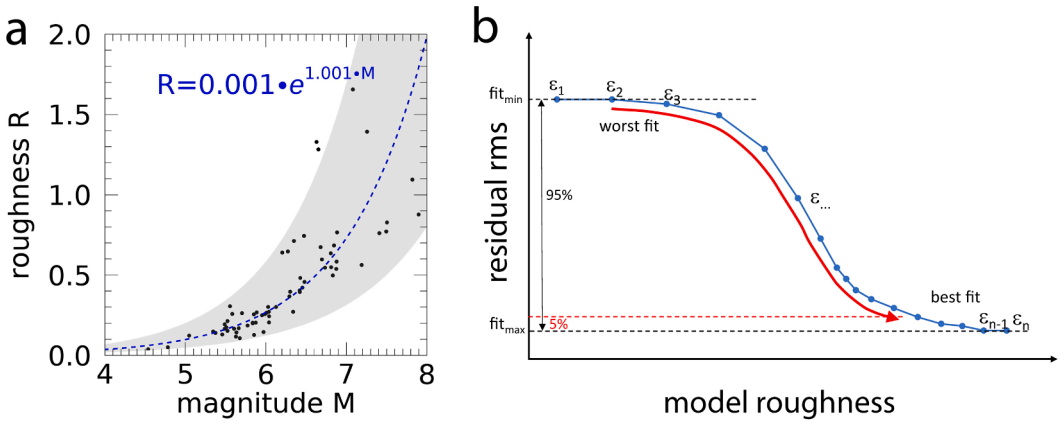

Fig. 6. (a) roughness vs. magnitude, for events successfully inverted, fitted with an exponential function; the grey area is defined by the R function with $+1\sigma$ and -1σ applied to the two free parameters; b) typical data fit vs. model roughness trade-off curve, built with decreasing damping factors $\varepsilon_1 \ldots \varepsilon_n$. Note that the worst-fit corresponds to over-smoothed solutions with a nearly uniform slip and the best fit to unrealistically scattering slip values.

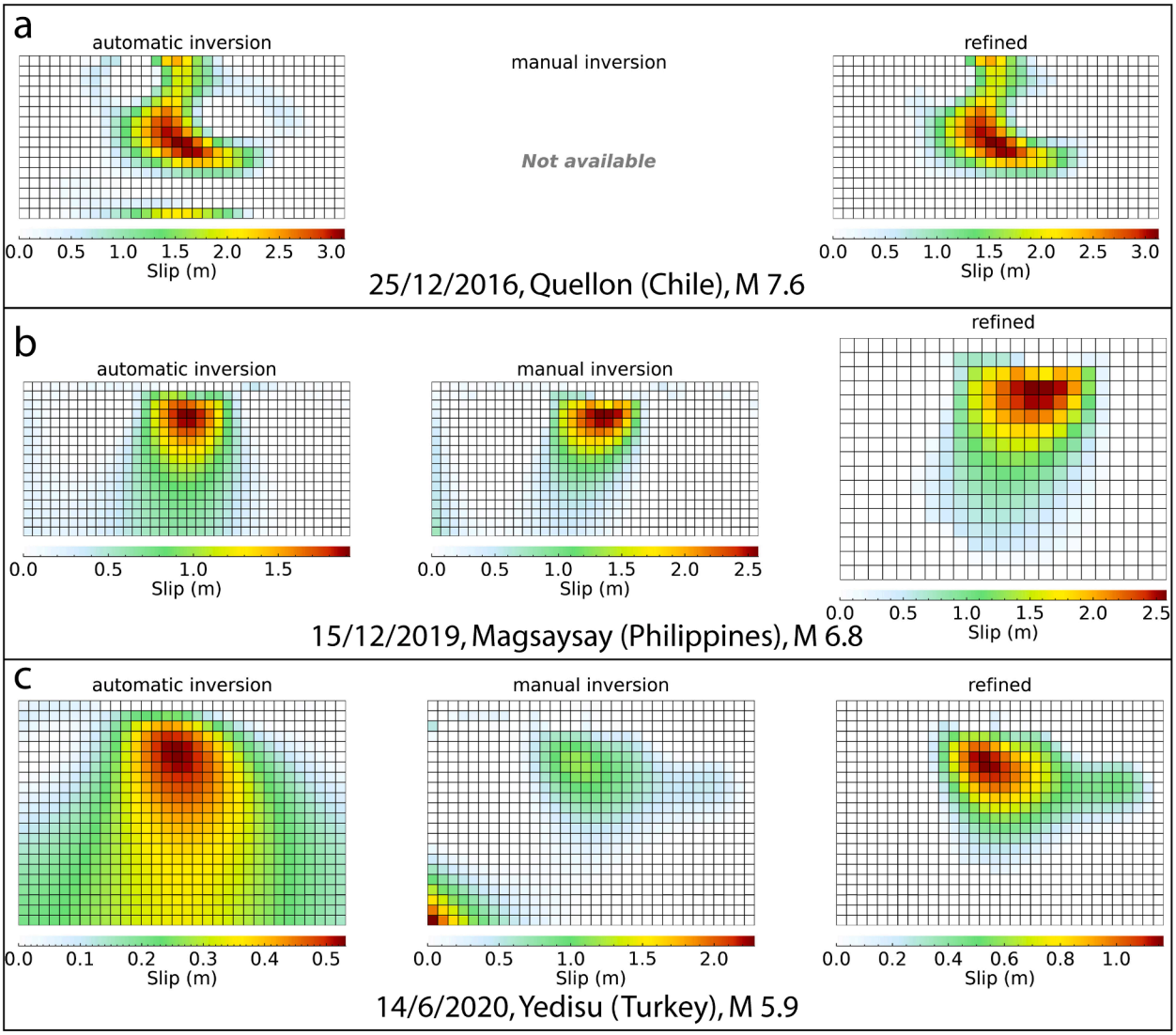

Fig. 7. Three examples of interactive refinement following the automatic inversion: (**a**) artifact removal without a manual inversion; (**b**) damping adjustment with manual inversion and cropping of the final fault; (**c**) damping adjustment with manual inversion and slip artifacts removal.

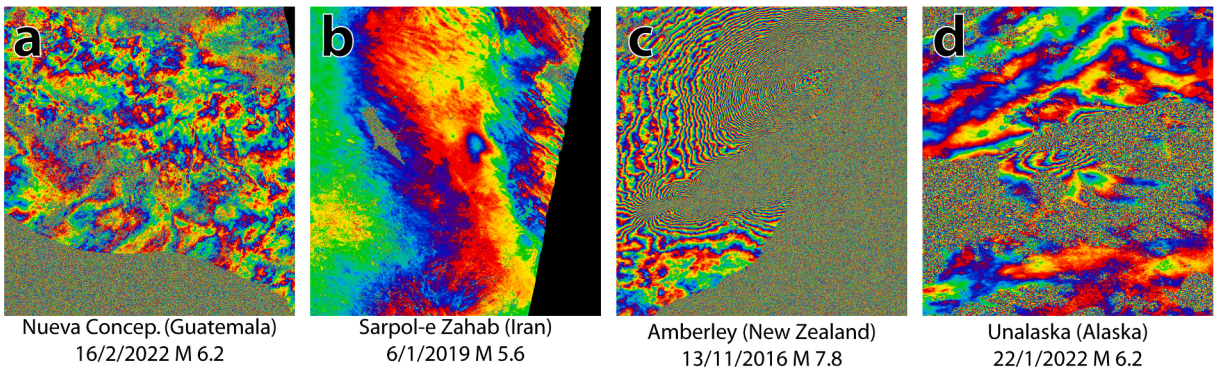

Fig. 8. Examples of algorithm failure due to (**a**) absence of coseismic signal, (**b**) presence of a very small signal, (**c**) signal complexity and (**d**) strong decorrelation inducing unwrapping errors.

1. the longest between length and width is subdivided into a predefined number of patches (30, by default);
2. the patch dimension is rounded to a multiple of hundreds/thousands of meters;
3. the number of patches in the other dimension is calculated;
4. final width and length are adjusted to be multiple of the patch size.

We remark that the overall goal is to provide a near real-time solution: we do not consider, in the current implementation, elements of variable size, according to the "full-resolution" algorithm presented in Atzori and Antonioli (2011) and Atzori et al. (2019).

6.2. System damping, data fit, model roughness

The slip distribution is carried out with a bounded, weighted and damped least-square inversion. Output parameters are calculated through:

$$\mathbf{m}^{est} = [\mathbf{G}^T\mathbf{W}_e\mathbf{G} + \varepsilon^2\mathbf{W}_m]^{-1}\ \mathbf{G}^T\mathbf{W}_e\mathbf{d} = \mathbf{G}^{-g}\mathbf{d}$$

where $\mathbf{m}^{est}$ is the array of slip values estimated from the inversion, $\mathbf{d}$ is the array of observed data, $\mathbf{G}$ is the design matrix, $\mathbf{W}_e$ is a data weighting matrix, $\mathbf{W}_m$ is the parameter weighting matrix, based on the Laplacian operator, and ε is the damping factor controlling the importance of $\mathbf{W}_m$ (Menke, 1989). The solution is also subject to the further constraint of non-negativity, to prevent back-slip values. In the current implementation, the design matrix $\mathbf{G}$ accounts only for a fixed rake, a condition that already gives reliable results for most of the moderate earthquakes and for several strong as well. A generalization to include a variable rake is out of the goal of the current implementation, but is straightforward from the technical point of view.

In the above equation, the $\mathbf{W}_e$ matrix contains the weight for each observed point and derives from the inverse of the data variance–covariance matrix $cov(\mathbf{d})$; the weight given to each dataset, instead, is the same calculated during the refined non-linear inversion. For sake of completeness, the design matrix $\mathbf{G}$ accounts also for the presence of offset (with one dataset) or a ramp affecting the InSAR datasets; for these parameters, appended to $\mathbf{m}^{est}$ vector, the non-negativity constraint is not applied.

In the above equation, a crucial role is played by the damping factor, that represents the strength of the slip regularization. A high number of approaches for an automatic calculation has been proposed in literature; nevertheless, ε is an inherently empirical parameter (Menke, 1989) and none of the proposed approaches could claim to have a general validity, though some of them, like the analysis of the data misfit vs. model roughness trade-off curves, are widely used. We adopt, for this project, a slightly different approach, still based on data fit and slip roughness.

We firstly observe the existence of a trend between the slip roughness and the event magnitude, that can be reasonably approximated with an exponential function (Fig. 6a); this relation is not influenced by the specific fault discretization and it allows to predict the roughness as function of the event magnitude.

In addition, fit/roughness curves always show a sigmoid pattern, limited between the worst and the best data fit (Fig. 6b), corresponding, respectively, to an overdamped and nearly uniform-slip solution and to a slip distribution characterized by unreliable jumps between adjacent patches.

According to these observations, the algorithm to define the damping factor ε follows these steps:

1. a data fit vs. model roughness curve is calculated to define, for the specific event, fit_{min} and fit_{max}, i.e. the worst and best fit values, respectively;
2. the damping factor is set to the value corresponding to 95% of the fit_{min}-fit_{max} interval;
3. the roughness of this slip distribution is compared to that expected from the roughness vs magnitude curve; if it is lower, damping is still decreased until the expected roughness value is reached.

This implementation allows to get, for most of the handled events, an acceptable solution. However, as far as a completely automatic and unsupervised result cannot be shared with the scientific community without any validation, we also developed a suite of graphical interfaces to allow an interaction with an expert operator, who can inspect the results and make, if necessary, quick adjustments before publishing the source model in a repository.

The description of these tools is off topic, but we briefly mention possible actions performed in this interactive phase:

1. *manual inversion refinement*: the input setting of the automatic inversion is adjusted, by changing the damping factor and/or the patch dimensions, and the linear inversion run again;
2. *slip distribution refinement*: large areas of zero slip or isolated artifacts induced by non-seismic signals are removed. Any slip change is followed by a forward modeling to inspect its impact on the predicted signal and on the observed-modeled residuals; after that, the modification is accepted or rejected (Fig. 7).

Source models are then published with the datasets used in the inversion in ESRI shapefile format, containing the observed, modeled and residual values as attributes.

7. Algorithm performance discussion

This implementation of the automatic inversion has been tested with 100 events, in a magnitude interval between 5.5 and 8.2, all picked from the EPOSAR catalog: this group of events describes an exhaustive record of configurations, mechanisms and InSAR displacements quality and

Table 1
List of the hundred events used in this work. The column "#" specifies the number of InSAR datasets used for source modeling, selected among those produced by the EPOSAR service. The slip distributions for successful outcomes are shown in the Supplementary Figure S1, while data and images can be accessed at http://terremoti.ingv.it/finitesource.

Name	#	M	Date	outcome	Name	#	M	Date	outcome
Lefkada (Greece)	2	6.5	17/11/2015	SUCCESSFUL	Magsaysay (Philippines)	2	6.8	15/12/2019	SUCCESSFUL
Murghob (Tajikistan)	4	7.2	7/12/2015	strong decorrelation	Gilgit (Pakistan)	4	5.6	30/12/2019	signal too small
Yujing (Taiwan)	1	6.4	5/2/2016	source complexity	Maria Antonia (Puerto Rico)	2	6.4	7/1/2020	SUCCESSFUL
Port Heiden (Alaska)	2	6.2	2/4/2016	strong decorrelation	Kashgar (China)	2	6.0	19/1/2020	SUCCESSFUL
Kumamoto (Japan)	4	7.0	15/4/2016	strong decorrelation	Karkaaa (Turkey)	4	5.6	22/1/2020	SUCCESSFUL
Muisne (Ecuador)	1	7.8	16/4/2016	SUCCESSFUL	Karakenja (Tajikistan)	1	5.5	24/1/2020	SUCCESSFUL
Chipinge (Zimbabwe)	2	5.6	22/9/2016	SUCCESSFUL	Doganyol (Turkey)	2	6.7	24/1/2020	SUCCESSFUL
Preci (Italy)	2	6.6	30/10/2016	source complexity	Salmas (Iran)	4	5.8	23/2/2020	source complexity
Amberley (New Zealand)	1	7.8	13/11/2016	source complexity	Kanalaki (Greece)	2	5.7	21/3/2020	SUCCESSFUL
Amberley (New Zealand)	4	5.5	22/11/2016	SUCCESSFUL	Stanley (Idaho)	2	6.5	31/3/2020	strong decorrelation
Reuleuet (Indonesia)	2	6.5	6/12/2016	SUCCESSFUL	Mohr (Iran)	2	5.5	9/6/2020	SUCCESSFUL
Quellon (Chile)	4	7.6	25/12/2016	SUCCESSFUL	Yedisu (Turkey)	4	5.9	14/6/2020	SUCCESSFUL
Daigo (Japan)	2	5.9	28/12/2016	SUCCESSFUL	Santa Maria Xadani (Mexico)	1	7.4	23/6/2020	SUCCESSFUL
Turkey West coast (Turkey)	4	5.5	6/2/2017	SUCCESSFUL	Hotan (China)	2	6.3	25/6/2020	SUCCESSFUL
Torbat-em (Iran)	2	6.1	5/4/2017	SUCCESSFUL	Western Xizang (China)	2	6.3	22/7/2020	SUCCESSFUL
Lim-oo (Philippines)	1	6.5	6/7/2017	strong decorrelation	San Pedro (Philippines)	1	6.6	18/8/2020	wrong model
San Pedro (Philippines)	1	5.8	10/7/2017	signal not visible	Neon Karlovision (Greece)	4	7.0	30/10/2020	SUCCESSFUL
Mawu (China)	2	6.5	8/8/2017	SUCCESSFUL	Turt (Mongolia)	1	6.7	11/1/2021	source complexity
Chiapas (Mexico)	2	8.2	8/9/2017	SUCCESSFUL	Lethem (Guyana)	2	5.5	31/1/2021	strong decorrelation
Matzaco (Mexico)	2	7.1	19/9/2017	signal too small	Tyrnavos (Greece)	4	6.3	3/3/2021	SUCCESSFUL
Ixtepec (Mexico)	2	6.1	23/9/2017	SUCCESSFUL	Elassona (Greece)	4	5.6	12/3/2021	SUCCESSFUL
Halabja (Iraq)	2	7.3	12/11/2017	SUCCESSFUL	Bandar-e Genaveh (Iran)	2	5.8	18/4/2021	SUCCESSFUL
Shi Yomi (India)	2	6.4	17/11/2017	strong decorrelation	Dali (China)	2	6.1	21/5/2021	SUCCESSFUL
Kerman (Iran)	2	6.1	1/12/2017	SUCCESSFUL	Southern Qinghai (China)	1	7.3	21/5/2021	SUCCESSFUL
Kerman (Iran)	2	6.0	12/12/2017	strong decorrelation	Antelope Valley (CA)	2	6.0	8/7/2021	SUCCESSFUL
Mandali (Iraq)	4	5.5	11/1/2018	SUCCESSFUL	Nippes (Haiti)	2	7.2	14/8/2021	strong decorrelation
Hualien City (Taiwan)	1	6.4	6/2/2018	SUCCESSFUL	Acapulco (Mexico)	2	7.0	8/9/2021	SUCCESSFUL
Pinotepa de Don Luis (Mexico)	2	7.2	16/2/2018	SUCCESSFUL	Mount Buller (Australia)	1	5.9	21/9/2021	signal not visible
Tari (Papua New Guinea)	2	7.5	25/2/2018	strong decorrelation	Thrapsanon (Greece)	4	6.0	27/9/2021	SUCCESSFUL
Leilani Estates (Hawaii)	2	6.9	4/5/2018	source complexity	Bandar Abbas (Iran)	1	6.0	14/11/2021	SUCCESSFUL
Labuan Lombok (Indonesia)	2	6.4	28/7/2018	SUCCESSFUL	Petrolia (CA)	2	6.2	20/12/2021	signal not visible
Labuan Lombok (Indonesia)	2	6.9	5/8/2018	SUCCESSFUL	Jinchang (China)	2	6.6	7/1/2022	SUCCESSFUL
Labuan Lombok (Indonesia)	2	6.9	19/8/2018	SUCCESSFUL	Pulau-Pulau Talaud (Indonesia)	1	6.0	22/1/2022	signal not visible
Bam (Iran)	1	5.6	7/9/2018	signal too small	Unalaska (Alaska)	1	6.2	22/1/2022	signal not visible
Rikaze (China)	2	5.8	23/12/2018	SUCCESSFUL	Laojunmiao (China)	1	5.6	23/1/2022	SUCCESSFUL

(continued on next page)

Table 1 (*continued*)

Name	#	M	Date	outcome	Name	#	M	Date	outcome
Sarpol-e Zahab (Iran)	4	5.6	6/1/2019	signal too small	Namuac (Philippines)	1	5.5	13/2/2022	signal not visible
Planadas (Colombia)	2	5.5	28/1/2019	signal too small	Nueva Concepcion (Guatemala)	1	6.2	16/2/2022	signal not visible
Paucarbamba (Peru)	2	5.5	14/2/2019	signal not visible	Laojunmiao (China)	2	5.7	25/3/2022	SUCCESSFUL
Volcano (Hawaii)	2	5.5	13/3/2019	signal not visible	Khst (Afghanistan)	2	5.9	21/6/2022	SUCCESSFUL
Labuan Lombok (Indonesia)	2	5.6	17/3/2019	signal not visible	Bandar-e Lengeh (Iran)	2	6.0	1/7/2022	SUCCESSFUL
Acipayam (Turkey)	4	5.7	20/3/2019	SUCCESSFUL	Dolores (Philippines)	1	7.0	27/7/2022	SUCCESSFUL
Ridgecrest Sequence	2	7.1	6/7/2019	SUCCESSFUL	Kangding (China)	1	6.6	5/9/2022	signal not visible
Masjed Soleyman (Iran)	2	5.6	8/7/2019	signal not visible	Aguililla (Mexico)	1	7.6	19/9/2022	SUCCESSFUL
Bomdila (India)	1	5.5	19/7/2019	signal not visible	Lebu (Chile)	2	6.2	13/11/2022	signal not visible
San Antonio (Chile)	1	6.8	1/8/2019	SUCCESSFUL	Duzce (Turkey)	2	6.1	23/11/2022	SUCCESSFUL
Baklan (Turkey)	2	5.9	8/8/2019	signal too small	Adigrat (Ethiopia)	2	5.5	26/12/2022	SUCCESSFUL
Shijak (Albania)	1	5.6	21/9/2019	signal not visible	Uzunbag (Turkey)	2	6.3	20/2/2023	SUCCESSFUL
Bulatukan (Philippines)	1	6.5	31/10/2019	strong decorrelation	Murghob (Tajikistan)	2	6.8	23/2/2023	SUCCESSFUL
Chiang Klang (Thailand)	2	5.7	20/11/2019	signal not visible	Umbertide (Italy)	2	4.3	9/3/2023	SUCCESSFUL
Mamurras (Albania)	2	6.4	26/11/2019	SUCCESSFUL	Maca (Peru)	2	5.5	3/6/2023	SUCCESSFUL

coverages. An additional small magnitude, the Mw 4.5 earthquake occurred near Umbertide (Italy) on March 9, 2023, is also included, to test the manual triggering of the InSAR automatic processing and modeling.

We firstly describe the processing failures, ended without providing any distributed slip model. Of the hundred events, 16 failed because the input data did not contain any visible coseismic pattern (Fig. 8a); we included these tests to check the system's ability to avoid false positives, since EPOSAR service is activated on the base of the event magnitude and depth and, for low or moderate magnitudes ($\lesssim 6$), the signal absence is commonly verified. In 6 cases the coseismic signal was very small, with intensity comparable to ordinary InSAR disturbances (Fig. 8b); for these cases, automatic modeling can fail because a misplacement of the starting focal mechanism leads to a wrong definition of the area of interest or because atmospheric artifacts dominate over the real signal. Within non-linear inversion, modeling the wrong signal pattern generally violates the convergence criterion 2 described in Section 5; in this case the linear inversion does not start. In other 6 cases, the deformation signal was too complex to be modeled with a single source; this occurred either for the rupture of different fault segments (Fig. 8c) during the same earthquake, or when earthquakes occurs in the same area but in different moments/days, or for the presence of multiple phenomena, like earthquakes and eruptions, as for Hawaiian events. Modeling multiple sources in an automatic way is currently not implemented, due to its complexity, and sources must be produced with standard modeling. For the sake of completeness, in the case of events occurred in different days, the EPOSAR service is triggered just once; in the catalog, the multi-source model is then replicated for all the interested earthquakes. Automatic figure captions are also manually edited to describe these specific conditions.

In 11 cases, modeling failed because the displacement maps were affected by strong decorrelation, due to the presence of water, snow or vegetation, leading to to phase unwrapping artifacts.

In 60 cases the modeling process successfully ended with the retrieval of a reliable slip distribution, eventually just needing the interactive refinements described above. For a complete list of the outcomes, see Table 1.

The validation of a slip distribution produced in real time from InSAR

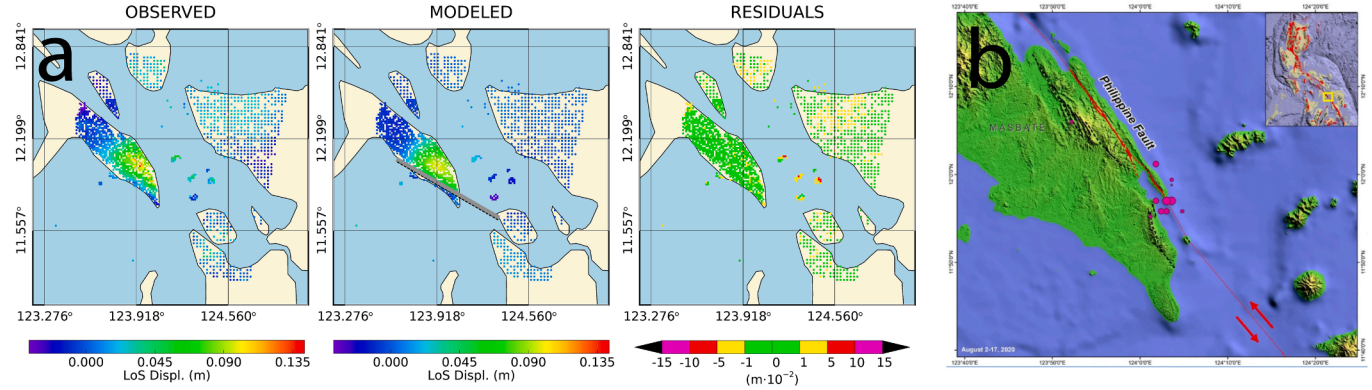

Fig. 9. Observed, modeled and residuals after the automatic inversion for the August 18, 2020, San Pedro (Philippines) M 6.6 event. The nearly vertical fault is misplaced, as visible by comparing the modeled solution (**a**) with the actual fault location (**b**, from Phivolcs, the Philippine Institute for Volcanology and Seismology).

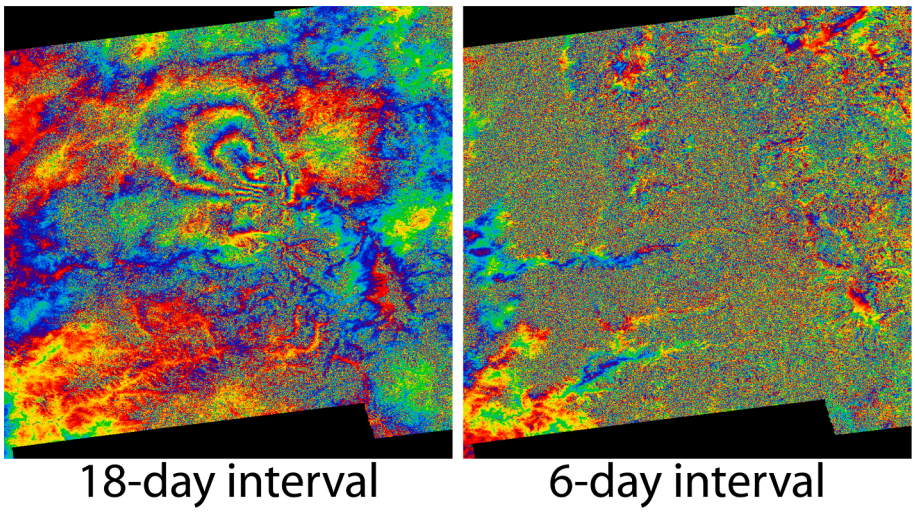

Fig. 10. Interferogram of the March 31, 2020, Stanley (Idaho) M 6.5 event, with 18-day (March 20 - April, 7) and 6-day (March, 26 - April, 1) temporal baselines. The drop of coherence is likely due to the presence of snow in one of the acquisitions constituting the 6-days pair.

data is conducted by the experts responsible for its publication and the user can inspect a comparison between the observed and predicted InSAR data, provided together with the slip distribution. Since we assume no other solutions from geodesy are available at the time of the source publication, a comparison with sources from literature is out of the main goals of this work. However, for sake of completeness, we provide in the Supplementary Material a section to compare 10, of the 60 slip models, with analogous from peer-review journals and from the USGS site, that publishes in near real time solutions based on seismic waveforms inversion.

We discuss here the only event the automatic processed without violating any convergence criterion, successfully ending with a reliable slip distribution, but with a mislocated fault plane (Fig. 9). A condition like this, which is relevant to the August 18, 2020, San Pedro (Philippines) M 6.6 event, is very unlikely; moreover, only one orbit was available and an additional one would have possibly prevented this wrong solution.

We further remark that a problem only partially addressed in the current implementation is related to the discrimination of the real from the auxiliary fault plane, since a focal mechanism is used as input. Apart from the interactive phase with an operator, who can manually set the real plane, an *ad hoc* algorithm to automatically do that has not yet been implemented. Discriminating the real from the auxiliary plane is mainly related to the ratio between the source depth and its dimension; as rule of thumb, when this ratio is about $4 \div 5$, the finiteness has no impact on the surface displacement pattern and a point-source already well predicts observed data. Under this condition, only external constraints can be used to define the real plane. As the depth/dimension ratio gets lower, the real plane provides a better data fit than the auxiliary one; in 29 of the 60 successful cases, the system failed to provide a slip distribution for the auxiliary plane, thus showing an implicit early-stage ability of discriminating the real from the auxiliary plane.

A final observation is about the InSAR pair selection algorithm, described above. By assuming that the Sentinel-1 orbital tube is generally narrow, the selection of the best pair for a given track is only based on the temporal baseline. Only for the March 31, 2020, Stanley (Idaho)

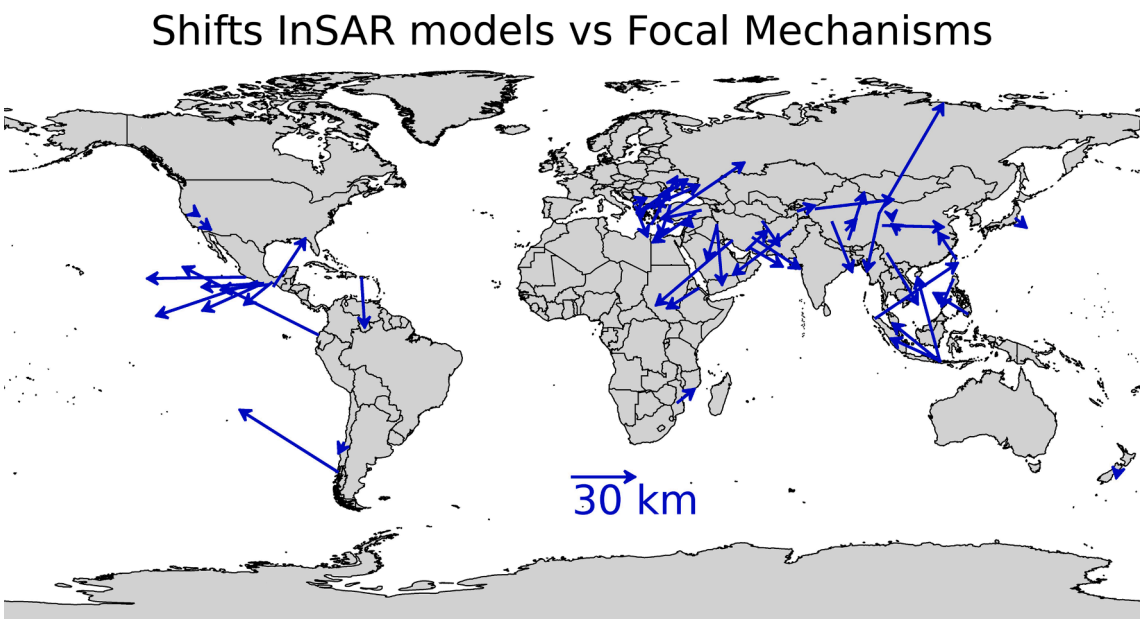

Fig. 11. Horizontal shifts between the USGS focal mechanism centroids and the barycenters of the slip distributions retrieved via linear inversion (arrow lengths not in scale with the map) for all the events considered in this work.

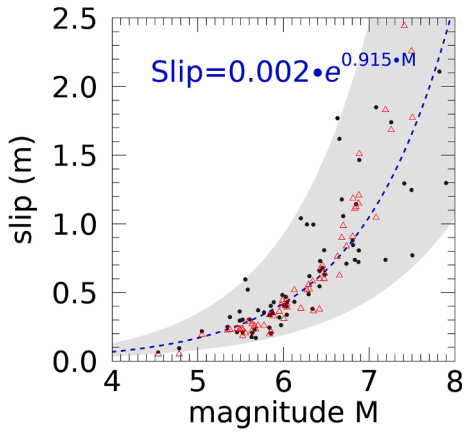

Fig. 12. Average slip as function of magnitude. The plot is based on the mean slip calculated for the slip distributions from the automatic inversion procedures (black dots). Red triangles are the mean slip values from the scaling factors of Leonard (2010). The gray area defines the exponential function +1 σ and −1 σ values added to the two free parameters.

M 6.5 event this implementation resulted to be not appropriate; the coherence of a 18-day pair shows higher values than that of 6-day (Fig. 10). This difference, affecting mountainous areas, is likely to occur for the presence of snow in one of the two images of the 6-day interval. Marginal situations like that are still not automatically handled in our implementation, thus requiring further developments; indeed, they can be managed by adding new constraints that accounts also for the spatial coherence.

8. Perspectives and conclusions

We managed to set up the first implementation of an algorithm for a fully automatic modeling of the seismic source parameters and the slip distribution, through the inversion of InSAR displacements. To do this, we exploited the InSAR processing chain developed by IREA-CNR and running through the EPOSAR service, and the procedures for the seismic source modeling developed at INGV. The whole processing chain has been tested for a hundred events and resulted successful for 60 cases. By excluding the 16 events for which InSAR measurements did not show any coseismic signal, the percentage of success rises to 71%. In all these cases, the resulting slip distributions only needed the refinement from an expert user, before becoming available to the scientific community.

In addition to the algorithmic aspects discussed in this work, we briefly address some perspectives coming out from the availability of this new processing chain.

We have already started extending our analysis of all the events that produced a deformation signal since the launch of the first Sentinel-1 satellite (April 2014). This is an ongoing work, involving about 200 earthquakes with magnitude above 5.5. Events with lower magnitude and showing a clear signal are also considered in the catalog, but their processing needs to be manually triggered. Sources and data will be made available through EPOS services, after the definition of their metadata, and through an *ad hoc* web portal; all these activities are under development. Sources and data can currently be retrieved in ESRI shapefile format through the INGV web page http://terremoti.ingv.it/finitesource. We remark that published sources are not presented as the best possible solutions, but as an instrument for a quick and robust identification of the source parameters after an earthquake. On the other hand, this repository will be exploited to store also refined and complex solutions published in peer-reviewed journals. In the event pages, results are presented with graphical images and relative captions.

Among the wide range of possible investigations allowed by the availability of a complete and homogeneous database of finite sources, we make here a couple of examples exploiting the successful outcomes of the 100 events processed for the presented automatic modeling implementation. An InSAR peculiarity, compared to seismological data, is the capability of defining the actual location of the event. Weston et al. (2011 and 2012) investigated this problem showing systematic shifts, in some regions, between the InSAR and the USGS locations. These results can be replicated and possibly deepened using this new catalog (Fig. 11); we already exploit systematic shifts to correct the scenarios based on the focal mechanisms, thus better centering the area of interest already for the coarse non-linear inversion.

Another potential topic emerging by the availability of a complete catalog is the inference of scaling factors to derive the finite fault parameters, that is important for a quick assessment of the event size from its moment magnitude and is largely faced in literature (Wells and Coppersmith, 1994; Leonard 2010, Thingbaijam et al 2017). In addition to the slip roughness, shown in Fig. 6a, we report here the expected average slip as function of the magnitude (Fig. 12), compared also with the average slip from scaling factor from Leonard (2010).

From an algorithmic point of view, the results of these two years of development are a starting point for a more complex automation of InSAR data analysis and modeling. Steps forward, easy to implement in a close future, are the inclusion of GNSS data (as those already provided within EPOS, according to Fernandes et al (2022)) and the rake unlocking for the retrieval of variable rake, slip distributions, especially for large earthquakes. A more challenging improvement will be the ability to include multi-segment sources, for which the adoption of AI-based procedures will be considered to face the exponential growth of complexity in the investigation of the free parameter space. Moreover, we plan to expose the results through i) *ad hoc* web services, in the framework of the EPOS infrastructure, and ii) in a dedicated web-portal, where databases of known active faults, like the DISS catalog (DISS working group, 2021) or the European Fault-Source Model 2020 (Basili et al., 2020, available at https://doi.org/10.13127/efsm20) and many others, will be included and, possibly, exploited for the stress transfer analysis through the Coulomb Failure Function (Harris, 1998).

A final consideration is about the data availability; while the opening of SAR data repositories (ALOS-1, Envisat, ERS-1 and 2) allows to extend the data analysis backward to more than 25 years of events, we impatiently wait for the incoming new and open access data with the incoming Sentinel-1C and NASA-ISRO SAR (NISAR) missions, planned to be operating in 2024. They will certainly allow us to further extend the system capabilities and performances for the real-time production of solutions.

Funding

This research was partially funded by the “Presidenza del Consiglio dei Ministri–Dipartimento della Protezione Civile” (Presidency of the Council of Ministers–Department of Civil Protection), through the 2022-2024 IREA-DPC agreement, the EPOS-SP project of the European Union Horizon 2020 for Research and Innovation Program under Grant 871121, and the EPOS-ITALY Joint Research Unit.

CRediT authorship contribution statement

Simone Atzori: Visualization, Formal analysis, Investigation, Conceptualization, Methodology, Software, Data curation, Writing - original draft, Writing - review & editing. **Fernando Monterroso:** Investigation, Writing – original draft, Conceptualization, Data curation, Data curation, Software, Validation. **Andrea Antonioli:** Methodology, Investigation, Writing – original draft. **Claudio De Luca:** Software, Writing – original draft. **Nikos Svigkas:** Validation, Conceptualization, Writing – original draft. **Francesco Casu:** Funding acquisition, Writing – original draft. **Michele Manunta:** Supervision, Writing – original draft. **Matteo Quintiliani:** Software, Writing – original draft. **Riccardo Lanari:** Writing – original draft, Supervision.

Declaration of Competing Interest

The authors declare that they have no known competing financial interests or personal relationships that could have appeared to influence the work reported in this paper.

Data availability

Data will be made available on request.

Acknowledgements

Special thanks to Rita Di Giovambattista and Laura Scognamiglio (INGV), for actively supporting the project. Special thanks to the anonymous reviewers that fairly commented on the manuscript, allowing its strengthening and the correction of several errors. The contents of this paper represent the authors' ideas and do not necessarily correspond to the official opinion and policies of the "Presidenza del Consiglio dei Ministri - Dipartimento della Protezione Civile" (Presidency of the Council of Ministers – Department of Civil Protection). This work contains modified Copernicus Sentinel data 2015-2023.

Appendix A. Supplementary material

Supplementary data to this article can be found online at https://doi.org/10.1016/j.jag.2023.103445.

References

Atzori, S., Antonioli, A., 2011. Optimal fault resolution in geodetic inversion of coseismic data. Geophys. J. Int. 185, 529–538. https://doi.org/10.1111/j.1365-246X.2011.04955.x.

Atzori, S., Hunstad, I., Chini, M., Salvi, S., Tolomei, C., Bignami, C., Stramondo, S., Trasatti, E., Antonioli, A., Boschi, E., 2009. Finite fault inversion of DInSAR coseismic displacement of the 2009 L'Aquila earthquake (Central Italy). Geoph. Res. Lett. 36 (15) https://doi.org/10.1029/2009GL039293.

Atzori, S., Salvi, S., 2014. Land Applications of Radar Remote Sensing. InTech. https://doi.org/10.5772/57479.

Atzori, S., Antonioli, A., Tolomei, C., De Novellis, V., De Luca, C., Monterroso, F., 2019. InSAR full-resolution analysis of the 2017–2018 M>6 earthquakes in Mexico. Rem. Sens. Env. 234, 111461 https://doi.org/10.1016/j.rse.2019.111461.

Basili, R., Danciu, L., Carafa, M.M.C., Kastelic, V., Maesano, F.E., Tiberti, M.M., Vallone, R., Gracia, E., Sesetyan, K., Atanackov, J., Sket-Motnikar, B., Zupančič, P., Vanneste, K., Vilanova, S., 2020. Insights on the European Fault-Source Model (EFSM20) as input to the 2020 update of the European Seismic Hazard Model (ESHM20). Copernicus GmbH. https://doi.org/10.5194/egusphere-egu2020-7008.

Casu, F., Elefante, S., Imperatore, P., Zinno, I., Manunta, M., De Luca, C., Lanari, R., 2014. SBAS-DInSAR parallel processing for deformation time-series computation. IEEE J. Sel. Top. Appl. Earth Observ. Remote Sens. 7 (8), 3285–3296. https://doi.org/10.1109/JSTARS.2014.2322671.

Costantini, M., Rosen, P.A., 1999. A generalized phase unwrapping approach for sparse data, IGARSS'99 - Geoscience and Remote Sensing Symposium, 1999, vol. 1, pp. 267-269, https://doi.org/10.1109/IGARSS.1999.773467.

DISS Working Group (2021). Database of Individual Seismogenic Sources (DISS), Version 3.3.0: A compilation of potential sources for earthquakes larger than M 5.5 in Italy and surrounding areas. Istituto Nazionale di Geofisica e Vulcanologia (INGV). https://doi.org/10.13127/diss3.3.0.

EPOS, European Plate Observing System, [Online]. Available at https://www.epos-ip.org/tcs/satellite-data.

Fernandes, R., Bruyninx, C., Crocker, P., Menut, J.-L., Socquet, A., Vergnolle, M., Avallone, A., Bos, M., Bruni, S., Cardoso, R., Carvalho, L., Cotte, N., D'Agostino, N., Deprez, A., Andras, F., Geraldes, F., Janex, G., Kenyeres, A., Legrand, J., Ngo, K.-M., Lidberg, M., Liwosz, T., Manteigueiro, J., Miglio, A., Soehne, W., Steffen, H., Toth, S., Dousa, J., Ganas, A., Kapetanidis, V., Batti, G., 2022. A new European service to share GNSS Data and Products. Ann. Geophys. 65, 3, DM317. https://www.annalsofgeophysics.eu/index.php/annals/article/view/8776.

Fornaro, G., Franceschetti, G., Lanari, R., Rossi, D., Tesauro, M., 1997. Interferometric SAR phase unwrapping using the finite element method. IEE Proceedings-Radar, Sonar and Navigation 144(5), 266-274, https://doi.org/10.1049/ip-rsn:19971259.

Gabriel, A.K., Goldstein, R.M., Zebker, H.A., 1989. Mapping small elevation changes over large areas: differential radar interferometry. J. Geophys. Res. Solid Earth 94 (B7), 9183–9191. https://doi.org/10.1029/JB094iB07p09183.

Harris, R.A., 1998. Introduction to special section: Stress trigger, stress shadows, and implication for seismic hazard, J. Geophys. Res., 103(B10), 24,347–24,358, https://doi.org/10.1029/98JB01576.

Leonard, M., 2010. Earthquake fault scaling: self-consistent relating of rupture length, width, average displacement, and moment release. Bull. Seismol. Soc. Am. 100 (5A), 1971–1988. https://doi.org/10.1785/0120090189.

Mai, P.M., Thingbaijam, K.K.S., 2014. SRCMOD: An online database of finite-fault rupture models. Seismol. Res. Lett. 85 (6), 1348–1357. https://doi.org/10.1785/0220140077.

Manunta, M., De Luca, C., Zinno, I., Casu, F., Manzo, M., Bonano, M., Fusco, A., Pepe, A., Onorato, G., Berardino, P., De Martino, P., Lanari, R., 2019. The parallel SBAS approach for Sentinel-1 interferometric wide swath deformation time-series generation: algorithm description and products quality assessment. IEEE Trans. Geosci. Remote Sensing 57 (9), 6259–6281. https://doi.org/10.1109/TGRS.2019.2904912.

Marquardt, D.W., 1963. An algorithm for least-squares estimation of nonlinear parameters. J. Soc. Ind. Appl. Math. 11, 431–441. https://doi.org/10.1137/0111030.

Massonnet, D., Rossi, M., Carmona, C., Adragna, F., Peltzer, G., Feigl, K., Rabaute, T., 1993. The displacement field of the Landers earthquake mapped by radar interferometry. Nature 364 (6433), 138–142. https://doi.org/10.1038/364138a0.

Menke, W., 1989. Geophysical Data Analysis Discrete Inverse Theory. Academic Press, San Diego. https://doi.org/10.1016/B978-0-12-490920-5.X5001-7.

Monterroso, F., Bonano, M., De Luca, C., Lanari, R., Manunta, M., Manzo, M., Onorato, G., Zinno, I., Casu, F., 2020. A global archive of Coseismic DInSAR products obtained through unsupervised Sentinel-1 Data processing. Remote Sens. (Basel) 12 (19), 3189. https://doi.org/10.3390/rs12193189.

Monterroso, F., Bonano, M., De Luca, C., Lanari, R., Manunta, M., Manzo, M., Onorato, G., Zinno, I., Casu, F., 2022. Automatic generation of Sentinel-1 DInSAR co-seismic maps at global scale. IEEE 21st Mediterranean Electrotechnical Conference (MELECON) Palermo, Italy 2022, 460–463. https://doi.org/10.1109/MELECON53508.2022.9843041.

Monterroso, F., Bonano, M., De Luca, C., De Novellis, V., Lanari, R., Manunta, M., Manzo, M., Onorato, G., Valerio, E., Zinno, I., Casu, F., 2019. Unsupervised and automatic generation of DInSAR Co-seismic displacement maps by means of Sentinel-1 data, IGARSS 2019 - 2019 IEEE International Geoscience and Remote Sensing Symposium, 2019, pp. 9658-9661, https://doi.org/10.1109/IGARSS.2019.8898772.

Okada, Y., 1985. Surface deformation due to shear and tensile faults in a half-space. Bull. Seismol. Soc. Am. 75, 1135–1154. https://doi.org/10.1785/BSSA0750041135.

Thingbaijam, K.K.S., Mai, P.M., Goda, K., 2017. New empirical earthquake source-scaling laws. Bull. Seism. Soc. Am. 107 (5), 2225–2246. https://doi.org/10.1785/0120170017.

Torres, R., Snoeij, P., Geudtner, D., Bibby, D., Davidson, M., Attema, E., Potin, P., Rommen, B., Floury, N., Brown, M., Traver, I., Deghaye, P., Duesmann, B., Rosich, B., Miranda, N., Bruno, C., L'Abbate, M., Croci, R., Pietropaolo, A., Huchler, M., Rostan, F., 2012. GMES Sentinel-1 mission. Remote Sens. Environ. 120, 9–24. https://doi.org/10.1016/j.rse.2011.05.028.

Wells, D.L., Coppersmith, K., J,, 1994. New empirical relationships among magnitude, rupture length, rupture width, rupture area, and surface displacement. Bull. Seism. Soc. Am. 84 (4), 974–1002. https://doi.org/10.1785/BSSA0840040974.

Weston, J., Ferreira, A.M.G., Funning, G.J., 2011. Global compilation of interferometric synthetic aperture radar earthquake source models: 1. Comparisons with seismic catalogs. J. Geophys. Res. 116, B08408. https://doi.org/10.1029/2010JB008131.

Weston, J., Ferreira, A.M.G., Funning, G.J., 2012. Systematic comparisons of earthquake source models determined using InSAR and seismic data. Tectonophysics 532 (535), 61–81. https://doi.org/10.1016/j.tecto.2012.02.001.

Williams, C.A., Wadge, G., 1998. The effects of topography on magma chamber deformation models: application to Mt. Etna and radar interferometry. Geophys. Res. Lett. 25 (10), 1549–1552. https://doi.org/10.1029/98GL01136.

Wright, T.J., Lu, Z., Wicks, C., 2003. Source model for the M w 6.7, 23 October 2002, Nenana Mountain Earthquake (Alaska) from InSAR : NENANA MOUNTAIN SOURCE MODEL FROM INSAR. Geophys. Res. Lett. 30 (18) https://doi.org/10.1029/2003GL018014.